

Article

Optimization Design of a Winch Suction Underwater Dredging Robot Using Orthogonal Experimental Design

Lijun Wang ^{1,*}, Yehao Kang ¹, Yibo Wang ¹, Zeyong Zhao ¹, Liyang Shang ², Xiaona Song ¹, Donglai Xu ³
and Ruixue Cheng ^{3,*} 

¹ School of Mechanical Engineering, North China University of Water Resources and Electric Power, Zhengzhou 450045, China; kangyh5928@163.com (Y.K.); 13569210290@139.com (Y.W.); 18159309865@163.com (Z.Z.); songxiaona1@126.com (X.S.)

² Yellow River Machinery Co., Ltd., Yellow River Conservancy Commission, Zhengzhou 450006, China; 13598888532@139.com

³ School of Computing, Engineering and Digital Technologies, Teesside University, Middlesbrough TS1 3BX, UK; d.xu@tees.ac.uk

* Correspondence: wanglijun@ncwu.edu.cn (L.W.); r.cheng@tees.ac.uk (R.C.)

Abstract: In marine engineering and water conservancy projects, dredging often occurs due to silt accumulation, which can impede the long-term development of water ecosystems and water storage systems. To enhance dredging efficiency and the performance of dredging machines, a novel type of winch suction underwater dredging robot was designed. Computational fluid dynamics software was utilized to establish a fluid model of the robot's winch suction dredging device and conduct model simulation experiments. The simulation test results were used to investigate the factors influencing dredging performance and their impact laws. Five key factors—namely, the reamer rotational speed, reamer arrangement angle, water flow rate, inlet pipe diameter, and outlet pipe diameter—were selected for consideration. By setting up various sets of factor levels, the significant influence of different factors on dredging efficiency was examined. Analysis of variance was employed to analyse the results of the orthogonal experimental design, leading to the identification of optimal factor levels and the establishment of an optimal scheme group. The results of the optimal scheme were verified, demonstrating a 13.049% increase in dredging efficiency and a 19.23% decrease in power consumption of the sludge pump compared to the initial experimental setup. The performance of the optimal program surpassed that of all the experimental designs and met the design requirements.

Keywords: marine hydraulic engineering; dredging; winch suction; orthogonal experimental design



Citation: Wang, L.; Kang, Y.; Wang, Y.; Zhao, Z.; Shang, L.; Song, X.; Xu, D.; Cheng, R. Optimization Design of a Winch Suction Underwater Dredging Robot Using Orthogonal

Experimental Design. *J. Mar. Sci. Eng.*

2024, 12, 741. [https://doi.org/](https://doi.org/10.3390/jmse12050741)

10.3390/jmse12050741

Received: 7 April 2024

Revised: 24 April 2024

Accepted: 25 April 2024

Published: 29 April 2024



Copyright: © 2024 by the authors. Licensee MDPI, Basel, Switzerland. This article is an open access article distributed under the terms and conditions of the Creative Commons Attribution (CC BY) license (<https://creativecommons.org/licenses/by/4.0/>).

1. Introduction

In recent years, China's marine and water conservancy projects have experienced significant growth to address various needs such as water supply, irrigation, power generation, and environmental management. However, these projects face challenges due to sedimentation and siltation issues during operation [1–3]. Using the Xiaolangdi Reservoir as an example, data from October 2016 revealed substantial siltation, with estimates reaching 3.899 billion tons and 3.2573 million cubic meters using sediment balance and cross-sectional methods, respectively, representing 45% of the reservoir's design capacity [4].

The accumulation of silt has adverse effects, including reduced water flow rates, flow declines, and increased water levels leading to flood prevention and control hazards [5]. For instance, in the Gao Beidian sectional gate of the Tonghui River in Beijing city, during the nonflood season of 2023, the average daily flow rate decreased to 6.34 m³/s, compared to 10.80 m³/s in 2018 and 8.56 m³/s in 2021 [6]. Additionally, sediment deposition contributes to microbial proliferation, fish mortality, and the decay of aquatic grass, resulting in severe water pollution [7,8].

Currently, common dredging methods in China include manual dredging with water stoppage and dredging boat operations [9]. However, manual dredging is inefficient, hazardous, and economically unsound for most water conservancy projects due to operational difficulties and costs associated with water stoppage. Although dredging boats are more effective in natural watersheds, they face challenges in urban rivers or constrained spaces, limiting their efficacy.

Hence, the development of a versatile, compact, user-friendly, and adaptable underwater dredging robot is crucial. Such technology can significantly enhance dredging efficiency without necessitating water stoppages.

Underwater robots are categorized into manned and unmanned types, with the latter further classified into autonomous, remotely operated, and composite variations [10–12]. Given the specific context of this study, remotely operated underwater robots (ROVs) are employed. ROVs offer numerous advantages, including stable signal transmission, ease of manipulation, robust expandability, and straightforward maintenance. They represent the predominant type of underwater dredging robot utilized [13,14].

Typically, underwater dredging robots consist of three core components: a chassis moving device, a dredging apparatus, and a recovery mechanism. The primary distinction among various dredging robots lies in the design of the dredging device, along with variances in the recovery and control programs.

During the 1950s, the United States pioneered the use of cameras with transparent materials sealed into the seabed to capture underwater image data. This marked a significant advancement in underwater exploration and data gathering. In 1960, the U.S. achieved another milestone by developing the world's first generation of ROV-CURV1-type ROVs. These remotely operated vehicles were instrumental in combining efforts with the "Alvin" AUV to successfully recover hydrogen bombs from the seabed, marking the beginning of a new era in ROV development [15]. In 1985, there was a significant increase in the development of ROVs with intelligent capabilities, leading to full-scale development. In 1988, the Jason I-type ROV (Woods Hole Oceanographic Institution), which underwent successful sea trials. Subsequently, in 2002, the Institute achieved another breakthrough with the development of the Jason II-type ROV, which is capable of diving to depths of up to 6500 m, showing remarkable progress in underwater exploration technology [16]. Moving on to other global developments, Canada's Inuktun Services contributed to the ROV landscape with the Seamor ROV. Featuring a frame-type design and equipped with four thrusters and manipulators, the Seamor ROV has found its primary applications in underwater hull maintenance and inspections. Russia's Indel-Partner made significant strides in ROV technology with the Super GNOM Pro. This ROV, also designed with a frame-type structure, incorporated three magnetically coupled thrusters, scanning sonars, manipulators, and other advanced features. Its main applications include underwater monitoring and maintenance tasks, particularly in underwater nuclear power plants [17]. The United States VIDEORAY company developed the VideoRayExplorer type ROV, which primarily focused on underwater monitoring tasks. Characterized by its streamlined design, this type of ROV integrates sensors such as a magnetic compass and others within its body, enabling efficient underwater monitoring operations. These developments collectively showcase the continuous evolution and diversification of ROV technology for various underwater applications [18].

In 1981, a significant milestone was achieved when the Shenyang Institute of Automation and Shanghai Jiaotong University successfully collaborated to develop the "Sea Man No. 1" ROV. This marked China's inaugural independently developed operational ROV, equipped with a six-degree-of-freedom manipulator, among other features. By 1986, the project reached fruition with successful sea trials, demonstrating the capabilities of China's first operational ROV. With a maximum dive depth of up to 200 m, the "Sea Man No. 1" showcased China's growing prowess in underwater technology. In 2014, China continued its advancements in ROV technology, with Shanghai Jiao Tong University and other domestic research institutes jointly developing an updated version of the "Sea Man No. 1" ROV.

This iteration featured a streamlined design, indicative of ongoing improvements in design and functionality. Concurrently, Tongji University and other domestic research institutions collaborated to develop the “Seahorse”, a remarkable achievement, as it boasted a diving depth capability of 4500 m. Not only was it the deepest diving ROV in China at the time, but it also boasted the largest system size and showed the highest level of localization in ROV development within the country [19]. These developments underscore China’s commitment to advancing its capabilities in underwater exploration and technology.

ROV SRD-6EC (Ellicott Dredge Technologies, Baltimore, MD, USA), employs a crawler chassis and hydraulic drive system. It features a front reamer capable of breaking down silt, which is then suctioned away by corresponding pumps for transport to a silt reprocessing system. This innovation is poised to enhance dredging efficiency and precision.

Moreover, Toolbo (Toolbot Robotics, Rotterdam, The Netherlands), which utilizes an auger program. This remotely operated robot boasts a compact size, easy operation, precise movement, and environmentally friendly dredging capabilities.

Bull-ROV (DRAGFLOW and GEROTTO FEDERICO SRL, Campodarsego, Italy), a novel dredging robot that integrates heavy-duty dredging pumps with ROV technology. By incorporating a specially designed front brush, this system efficiently collects silt, which is then pumped directly to the suction inlet by heavy-duty dredging pumps. This design is particularly effective in handling situations with a high solid content in the silt.

The VVL-QY270-130A underwater dredging robot (Shandong Future Robotics Co., Weihai, China), utilizes a frame-type structure with a slurry pump winch suction dredging system, which features an all-hydraulic drive and cable-controlled operation. Its operational principle involves utilizing a spiral winch to gather silt and direct it towards the suction port. Subsequently, the collected silt is drawn in by the slurry pump and expelled to the water surface, facilitating efficient dredging operations.

On the other hand, the underwater automatic dredging robot developed by Shenzhen LAND Intelligent Robotics Co. incorporates automatic cable winding capabilities, enabling seamless automatic dredging operations across various water environments. This enhancement significantly boosts dredging efficiency. The specific structure of this underwater automatic dredging robot is illustrated.

Additionally, the KJBD-X03 dredging robot (Bodo Building Material Technology Co., Shenyang, China) can be outfitted with a professional muddy water camera for both monitoring and dredging tasks. Its proven reliability and stability over extended periods make it suitable for diverse water dredging applications.

This paper introduces a remotely operated vehicle (ROV) underwater dredging robot equipped with a movable winch suction device. A prototype of this robot is developed, allowing it to adjust the position of the winch suction device to optimize dredging efficiency under various underwater conditions.

To investigate the impact of different parameter settings on dredging efficiency and identify optimal parameters, a simulation model of a winch suction dredging device is established using CFD based on a three-dimensional model. Orthogonal experimental design was used to conduct simulation tests, and the results of the simulation tests were analysed by ANOVA to determine the optimal parameter data. Subsequently, the prototype model is optimized based on these parameters.

The novelty of this research lies in the rarity of underwater dredging robots employing movable suction dredging devices. The adaptability of the reamer, which can be adjusted to various positions to suit different underwater dredging environments, sets this robot apart.

Furthermore, the performance optimization method introduced in this paper offers several innovations: first, it efficiently selects a representative subset of experimental schemes from the entire set; second, it introduces superior schemes through statistical analysis of the results from this subset; and finally, it conducts further analysis of experimental results to glean additional insights beyond the raw data. These methodological advancements significantly contributed to the optimization process and enriched the findings of the study. The paper’s structure unfolds as follows: In Section 2, the structure of

the underwater winch suction dredging device and the simulation modelling method are described. Section 3 describes the selection of factors influencing dredging performance. Section 4 describes the orthogonal test design and analysis of variance (ANOVA) based on the test structure. It then proceeds to select the optimal scheme, verify its results, and ultimately determine the optimal scheme.

2. Computational Fluid Dynamics Model Building, Simulation and Verification

2.1. Basic Model Construction

After completing the preliminary design phase, the initial structure of the winch suction underwater dredging robot was established. The three-dimensional representation of this structure is depicted in Figure 1 below:

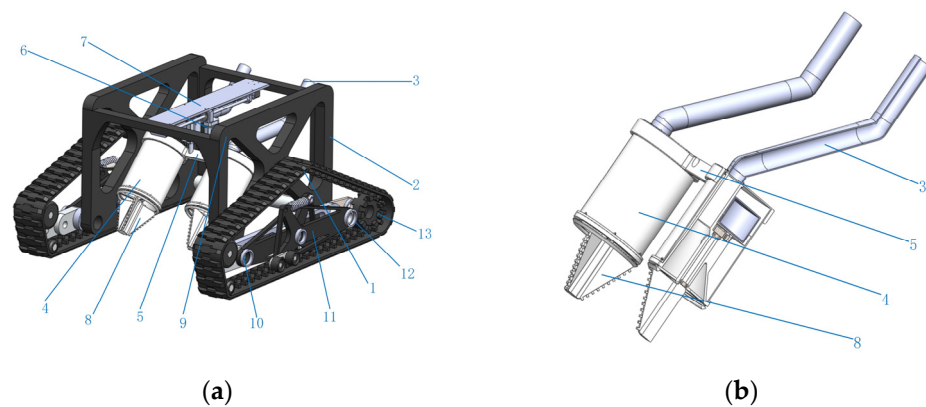


Figure 1. In the figure, 1—tracked chassis, 2—main frame, 3—mud pump pipe, 4—reamer device, 5—reamer connecting ring, 6—motorized actuator, 7—screw slide, 8—reamer, 9—sonar sensor, 10—front axle of the tracked chassis, 11—cushioning connecting member of the tracked chassis, 12—rear axle of the tracked chassis, and 13—motor of the tracked chassis. (a) Schematic diagram of the structure of the suction dredging robot. (b) Schematic diagram of the structure of the winch suction device.

To effectively utilize a winch suction dredging device for dredging tasks, an underwater robot requires both a control system and a power system. The control system facilitates real-time control of the underwater robot from the water surface, allowing adjustments to adapt to different underwater working conditions and enabling control over the start and end of the winch suction dredging process. The control mechanism on the water surface is connected to the robot through a range control system, ensuring seamless communication and operation.

The power system provides electricity to the reamer and motor of the underwater robot. A power cable connects the motor to the power supply, ensuring continuous power delivery for the operation of the robot's components. The reamer is responsible for dredging work underwater. The dredging process is initiated by mixing deposited silt and water through high-speed rotation. The reamer's start and end of dredging work are controlled by the control system. Positioned at the back end of the reamer device, the connection bin collects the mixture of silt and water churned by the front-end reamer. It serves as a transition point for the material before it enters the back-end pipeline. The back-end pipeline receives a mixture of silt and water from the connection bin and transports it to the shore for further processing.

Located on the water's surface, the sludge pump draws a mixture of silt and water from the back-end pipeline and transports it to the shore. This step completes the entire desilting workflow, efficiently removing sediment from underwater environments.

Based on the initial simulation experiment results and the observed issues, optimizing the winch suction device of the underwater dredging robot is crucial for achieving the highest theoretical dredging efficiency. In the initial simulation experiments, the reamer

rotation speed was set at 60 rpm, with a reamer arrangement angle of 45° (relative to the horizontal plane). The pump pipe outlet had a current speed of 1.3 m/s, with a connecting silo diameter of 168 mm and an outlet diameter of 56 mm. Through these tests, the desilting efficiency was approximately 0.83538. During the experimental process, it was observed that excessive reamer rotation speed led to the mixing of sludge and water, resulting in the spread of centrifugal force. Conversely, too slow flow in the pump pipe caused accumulation in the connecting bin, thereby decreasing the overall efficiency of suction dredging. Furthermore, an inadequate flow rate in the pump pipe led to silt accumulation in the connecting chamber, further decreasing the efficiency of winch suction dredging. Hence, optimization of the winch suction device is essential to achieve the highest theoretical dredging efficiency in the underwater dredging robot.

2.2. Computational Fluid Model Construction

Constructing a fluid model for performance optimization involves representing the three-dimensional structure of the suction dredging device, including the reamer, connecting warehouse, and pipeline, within the fluid domain. The device shell, which isolates the internal components from the water, creates a hollow structure within the fluid domain. Thus, it is crucial to include this part of the fluid domain in the model. Figure 2 illustrates the final determination of the fluid domain model. Once determined, the model will be imported into Fluent 2023R1 for preprocessing and processing. This involves setting boundary conditions, defining fluid properties, meshing the model, and specifying solver settings to simulate fluid flow behaviour accurately. By leveraging computational fluid dynamics (CFD) simulations in Fluent, engineers can analyse the performance of dredging devices, optimize their design parameters, and improve their efficiency in desilting operations. The fluid domain model dimensional parameters in Figure 2 are shown in Table 1.

Table 1. Dimensional parameters of the fluid domain model.

Parameters	Dimensions	Remarks
A	1000 mm	Length of fluid domain
B1	1000 mm	Height of fluid domain
B2	500 mm	Height of fluid inlet
C	1000 mm	Width of fluid domain
D1	56 mm	Diameter of outlet pipe outside
D2	48 mm	Diameter of outlet pipe inner
D3	70 mm	Diameter of the top surface of the rotating field
E1	200 mm	Housing diameter of the suction winch
E2	168 mm	Inlet diameter of suction winch
L1	273 mm	Housing length of the suction winch
L2	163 mm	Height of the rotating field
R	45°	Setting angle of the suction winch

The fluid domain is established as a 1 m square, with boundaries dividing it into water and silt regions above and below, respectively. The inlet boundaries for water and silt are defined as Inlet-shui and Inlet-mud, respectively, which are positioned around the four surfaces. A sliding mesh rotating domain, designated as a fan, is configured with three surfaces as interface surfaces. The internal wall of the winch suction device is labelled Wall-in, while the shell of the device is termed Wall-out. The outlet of the water surface pipe is defined as the outlet, with all other faces set as default walls, as shown in Figure 3:

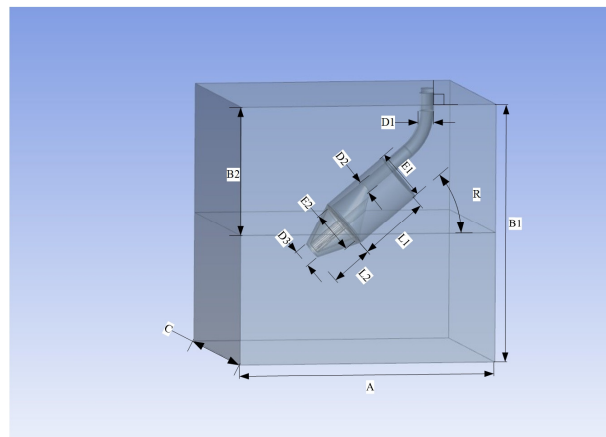


Figure 2. Dimensional parameters of the fluid domain model of the winches.

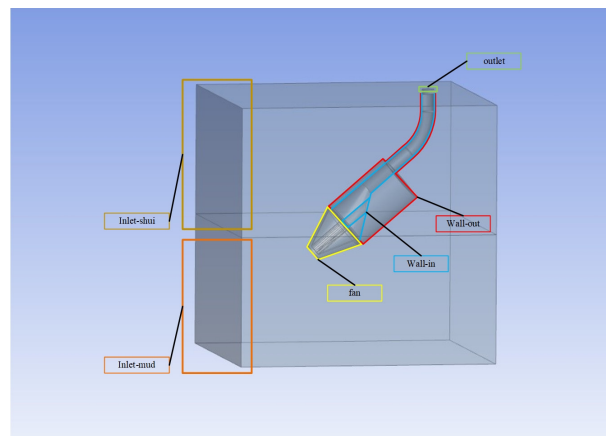


Figure 3. Definition of the parameters of the fluid domain model of the winch.

After setup, the model is imported into Fluent Meshing 2023R1 for tetrahedral meshing. The rotational domain and pipe meshing size is 5 mm, while other meshes are set to 20 mm. The resulting mesh model, illustrated in Figure 4, has an average mesh mass of 0.87 and a total of 765,986 meshes.

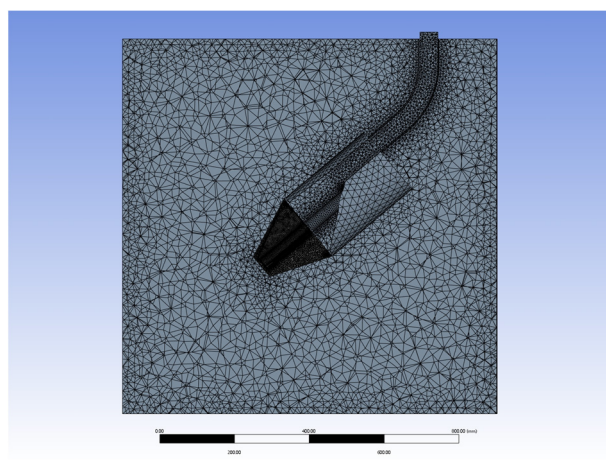


Figure 4. Cross section of fluid domain meshing model.

2.3. Computational Fluid Simulation Experiment Setup

In the material setup, the two fluids are liquid water and silt, the density of liquid water under standard conditions is $\rho = 1.030 \times 10^3 \text{kg/m}^3$, and the dynamic viscosity is $\mu = 1.61 \times 10^{-3} \text{kg/(m} \cdot \text{s)}$; by reviewing the relevant literature, the relevant parameters of the silt in different regions are shown in Table 2. The comprehensive consideration of the material parameters of the silt is selected as follows.

Table 2. Parameters of silt content in different areas.

	Density (kg/m ³)	Natural Moisture Content (%)	Viscous Particle Content (%)	Liquid Limit (%)	Plastic Limit (%)
Suzhou River Silt	1512	93.1	--	51.34	30.46
Nanjing Qinhuai River Silt	1351	86	16.7	45.27	29.52
Silt in Daya Bay, Shenzhen	1236	105	8	73.4	29.3
Mud on a beach in Taizhou	1212	168.6	2.74	--	35.2
Ningbo Offshore Mudflats	1210	90	2.64	46.5	26.3

From the silt parameters in the above table, it can be seen that the natural water content of the silt is greater than the liquid limit and plastic limit, the viscosity of the silt varies greatly with the water content, and the silt is in a flowing state. According to the silt data in the above table and the numerical models established by other scholars in silt simulation, the silt model adopted in this paper has a density parameter range of 1325–1375 kg/m³, a viscosity parameter range of 0.01–0.02, and a viscous particle content parameter range of 5–12%.

To solve the turbulence model selection, Fluent supports a variety of turbulence models to calculate the Reynolds number Re for the fluid domain model of the winch:

$$Re = \frac{\rho \cdot v \cdot L}{\mu} \tag{1}$$

where ρ is the density in kg/m³, v is the flow velocity in m/s, L is the characteristic length in m, and μ is the dynamic viscosity in kg/(m · s).

The Reynolds number (Re) at the inlet of the winch suction device exceeds 4000, indicating the need to select a turbulence model. Commonly employed turbulence models include the standard k-epsilon model, realizable k-epsilon model, RNG k-epsilon model, and RSM model. The standard k-epsilon model is renowned for its robustness and suitability for initial iterations, preliminary screening, and parameter studies. On the other hand, the realizable k-epsilon model is adept at handling complex shear flows with rapid strain and local transitional flows. Moreover, the RNG k-epsilon model is typically applied in cases involving strong rotation, albeit it may encounter convergence challenges.

In this study, the realizable k-epsilon model is chosen for the fluid simulation calculations due to its effectiveness in handling complex shear flows and local transitional flows.

Within the computational fluid domain, two fluids, water and silt, are selected for computation. Therefore, selecting a multiphase flow model becomes necessary. Options in Fluent include the VOF (volume of FLUID) model, mixture model, and Euler model. The VOF model is primarily used when dealing with fluid interfaces that do not intersect with each other. On the other hand, the mixture model is suitable for two-phase flow or scenarios involving more than three phases. It primarily solves the momentum equation of the mixture and then addresses discrete phase calculations based on the obtained velocity. While the Euler model yields good results in complex cases, particularly in fluidized bed and particle suspension calculations, it tends to have slower computing speeds and convergence challenges [20].

Considering computational efficiency and convergence concerns, the mixture model is selected for the fluid simulation in this paper, ensuring a balance between accuracy and

computational cost. In the fluid domain model of the winch suction device, the rotating domain fan necessitates rotation. Consequently, the boundary conditions of the rotating domain fan profoundly impact the stability of the data transmission between the rotating domain fan and the surrounding fixed fluid domain. As depicted in Figure 5, the three surfaces of the rotating domain fan are configured to form intersection interfaces with the surrounding fixed fluid domain. These interfaces are denoted as interface-1-A\B, interface-2-A\B, and interface-3-A\B, where face A represents the face of the rotating domain fan, and face B represents the face of the surrounding fixed domain.

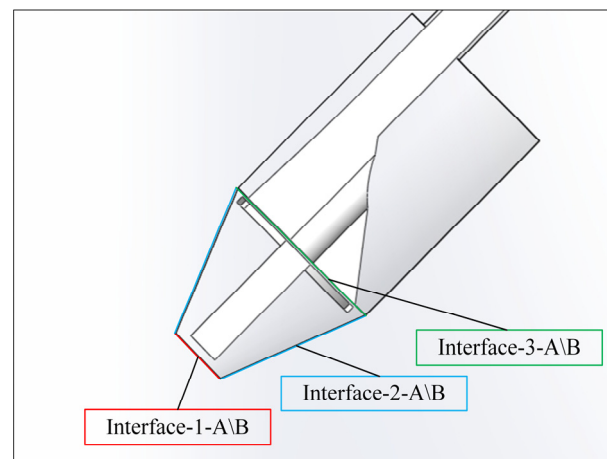


Figure 5. Interface setting diagram.

Once the computational model and boundary condition treatments are established, attention shifts to setting the solution parameters. Fluent offers two main solver types: pressure-based solvers and density-based solvers. Given that the density-based solver is typically reserved for high Mach number scenarios, it is not applicable to the model in this paper. Therefore, the default pressure-based solver in Fluent is adopted for the simulation and the remaining conditions, such as the residual convergence of 5^{-10} , the turbulent kinetic energy, the continuity requirements, the energy, and other convergence conditions are set to 3^{-10} .

3. Analysis of Factors Affecting Dredging Performance

In the simulation test of the winch suction device, it is crucial to determine the factors influencing dredging efficiency and establish the parameter range for experimentation. This paper utilizes the export volume fraction of silt in the slurry mixture as a benchmark. Analyses were conducted on five influencing factors: the rotational speed of the winch suction device reamer, the angle of arrangement of the winch suction device, the suction power of the sludge pump, the inlet diameter of the winch suction device, and the diameter of the pipeline of the mud pump.

3.1. Analysis of the Impact of Reamer Speed

The influence of the reamer speed on the dredging efficiency is illustrated in Figure 6. At a reamer speed of 120 rpm, the distribution of silt and water at various time intervals demonstrates the gradual mixing of mud with water propelled by the rotation of the reamer device. As the reamer rotates, centrifugal forces come into play, causing the mud to disperse outwards until it reaches a stable state of mixing with the water.

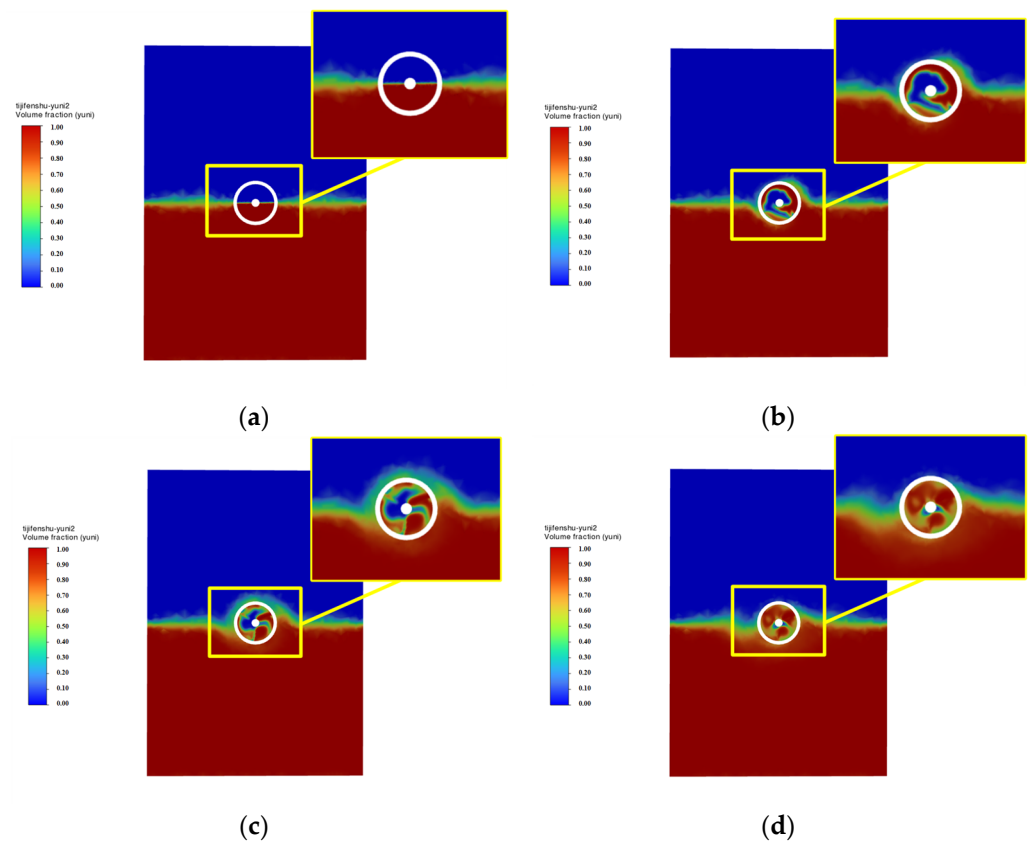


Figure 6. Volume of sludge at different moments of reamer speed 120 rpm. (a) Silt distribution in the initial moment. (b) Silt distribution at the 0.25 s moment. (c) Silt distribution at 0.5 s moment. (d) Silt at 0.75 s moment, respectively.

To validate the reliability of the simulation results, Figure 7 displays the velocity cloud of the reamer at 120 rpm. The maximum velocity observed is 1.25 m/s. This velocity can be corroborated using the equation for linear and angular velocities:

$$v = \omega \cdot r = \frac{2\pi \cdot n \cdot r}{60} \tag{2}$$

where v is the linear velocity, m/s; ω is the angular velocity, rad/s; r is the radius of rotation, 0.1 m; and n is the rotational speed, 120 rpm.

The calculated maximum linear velocity $v_{\max} = 1.26$ m/s, is consistent with the results of the velocity cloud diagram, indicating that the simulation results are reliable.

The rotational speed of the reamer on the winch suction device significantly influences dredging efficiency. Under the same pump suction power (resulting in identical water velocity), arrangement angle, and pipe diameter, varying rotational speeds yield different states of sludge mixing at the device inlet. At low rotational speeds, insufficient mixing occurs, with water predominating in the pumped-out mixture. At high rotational speeds, rapid and complete mixing transpires, but excessive centrifugal force causes widespread dispersion of the mixture, potentially polluting the water body. Only a limited amount of sludge can be pumped out under these conditions.

Determining the optimal rotational speed is crucial for achieving stable and efficient desilting operations. To determine this, a range of rotational speeds was tested incrementally with a gradient of 15 rpm. The interval between rotational speeds is determined based on changes in the silt volume fraction observed in simulation tests. The results of these tests are illustrated in Figure 8.

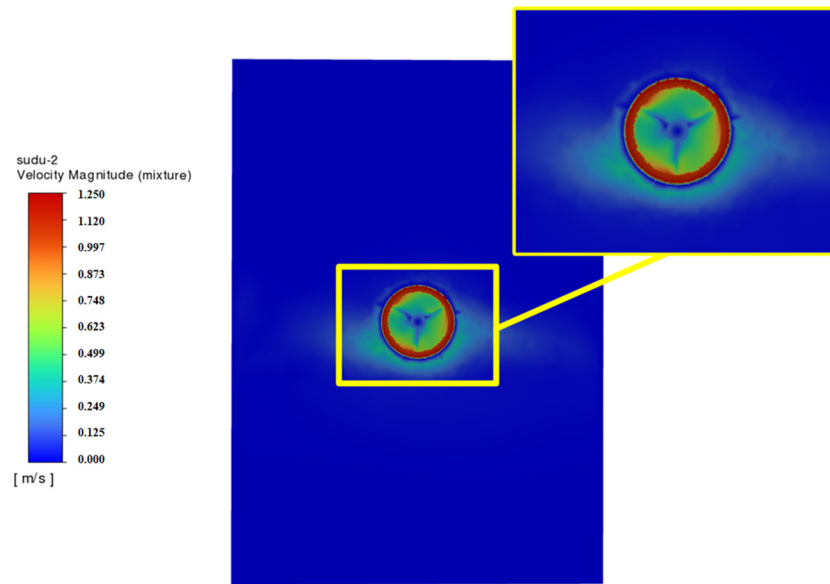


Figure 7. Reamer Speed 120 rpm Speed Cloud.

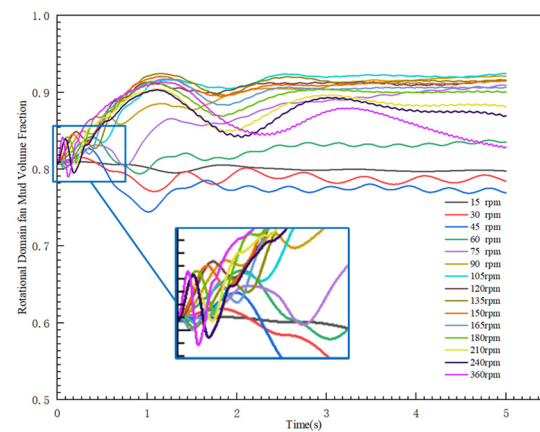


Figure 8. Silt volume fraction at different rotational speeds.

In Figure 8, the observations reveal distinct patterns based on the rotational speed intervals:
 At 15–60 rpm: The silt volume fraction fluctuates, suggesting uneven mixing.
 At 75–120 rpm: The silt volume fraction increases smoothly, indicating uniform mixing.
 At 150 rpm and above: The silt volume fraction initially increases but then sharply decreases with significant fluctuations, indicating that excessive centrifugal force leads to nonuniform mixing.

This analysis underscores the significant impact of varying reamer speeds on dredging efficiency.

3.2. Analysis of the Influence of the Arrangement Angle of the Winch Suction Device

The arrangement angle of the reaming device significantly affects dredging efficiency. This angle, defined as the angle between the centre axis of the reaming device and the interface of silt and water (ranging from 0° to 180°), determines how the rotating domain of the fan impacts the silt and water within it during each revolution.

Different arrangement angles lead to varying volume ratios of silt and water within the rotating domain of the fan, influencing the volume ratio affected by each revolution of the reamer. For instance, when the arrangement angle is 0°, which indicates alignment with the interface of silt and water, the volume ratio of silt and water in the rotating domain fan

is 1:1. Conversely, at an arrangement angle of 180°, all the silt within the rotating domain fan is affected.

Figure 9 illustrates these relationships, demonstrating that the error of the volume fraction ratio of silt and water in both the reamer and rotating domain models is within 1%. These findings emphasize the critical role of the arrangement angle in optimizing dredging efficiency.

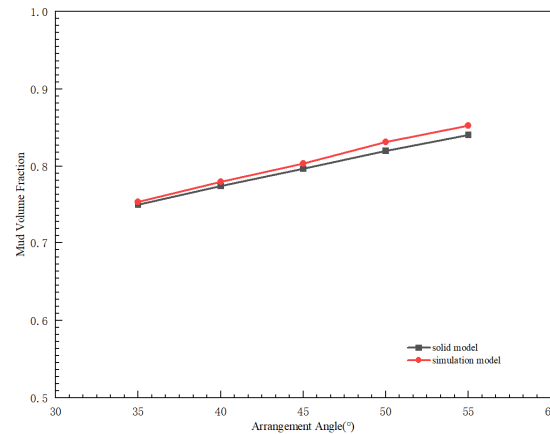


Figure 9. Comparison of silt volume between physical model and simulation model with different arrangement angles.

Aligned with the aforementioned reamer speed, the arrangement angle of the winch suction device plays a crucial role. With consistent pump power (thus, maintaining the same water flow rate), reamer speed, and pipeline diameter, the volume ratio of silt and water affected by each rotation of the reamer varies across different arrangement angles. Therefore, selecting an optimal arrangement angle is essential for ensuring stable and efficient desilting operations.

To explore this further, various arrangement angles are tested with a gradient of 5°. The arrangement angle of the reamer is then determined based on the changes in the volume fraction of silt. The results of these experiments are illustrated in Figure 10.

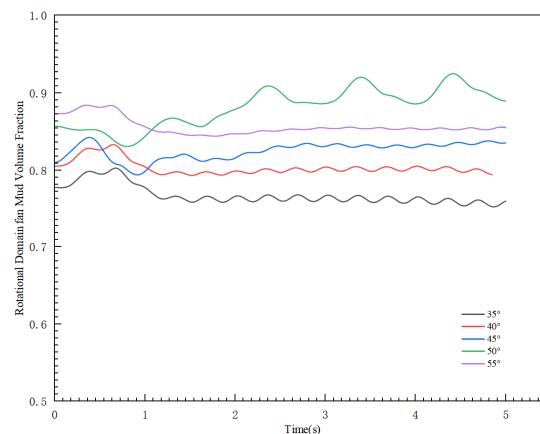


Figure 10. Silt Volume Fraction at Different Arrangement Angles.

In Figure 10, the silt volume fraction at the onset of the simulation varies across different arrangement angles of the winch suction device, which is consistent with the outcomes of the solid model. The curves exhibit a pattern of initial increase followed by a decrease for arrangement angles of 35°, 40°, 45°, and 55°, ultimately stabilizing. Conversely, when the arrangement angle is 50°, the curve initially decreases, then increases, and eventually stabilizes, albeit with indications of fluctuation.

Moreover, for arrangement angles of 35°, 40°, and 55°, the final silt volume fraction is lower than the initial state, while for bedding angles of 45° and 50°, the final silt volume fraction surpasses the initial state. This observation underscores the influence of varying arrangement angles of the winch suction device on dredging efficiency.

3.3. Analysis of the Impact of Mud Pump Power

The effect of the mud pump suction power (water velocity in the pipeline) on the dredging efficiency, according to the existing commercial pump parameters, can be calculated for a water velocity in the pipeline range of 0.7–2.1 m/s; the specific parameters of the pump are shown in Table 3.

Table 3. Pump parameters.

Illustration	Dimensions	Voltage	Flow Rate	Headlift
	332 × 160 × 190 mm	24 V	5–15 m ³ /h	5.5–11 m

At identical rotational speeds, arrangement angles, and pipe diameters, varying water velocities result in different mixing times for sludge at the inlet of the dredging device, leading to distinct mixing states. Higher water velocities cause incomplete mixing of sludge and water due to inadequate pump suction, exacerbated by larger impacts from bends in the pipeline’s inner wall. Conversely, lower water velocities lead to phenomena such as sludge accumulation at the pipeline mouth and potential clogging, along with larger fluctuations in speed at bends, resulting in a separation of the mixed state. Thus, determining an optimal water velocity is crucial for ensuring stable and efficient desilting operations with a winch suction device. The simulation test involves setting different water flow speeds with a gradient of 0.35 m/s, and selected results are illustrated in Figure 11.

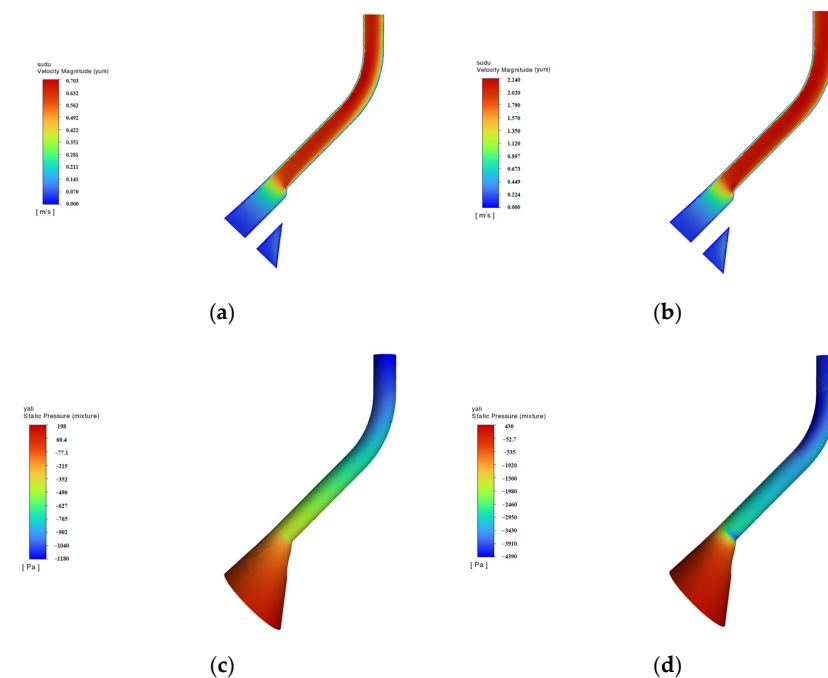


Figure 11. Velocity and pressure maps of the pipe for different water velocities. (a) Velocity distribution of water velocity 0.7 m/s. (b) Velocity distribution of water velocity 2.1 m/s. (c) Pressure distribution for water velocity 0.7 m/s. (d) Pressure distribution for water velocity 2.1 m/s.

According to the velocity cloud diagram in Figure 11, the fluid velocity decreases as the fluid enters the inlet conical pipe. At the junction of the conical and cylindrical pipes where the pipe diameter decreases, the velocity peaks, becoming more uniform within the straight section of the cylindrical pipe. However, within pipe bends, the velocity is greater near the inner bend and lower near the outer bend due to velocity fluctuations, resulting in energy loss and affecting the mixing state. Additionally, analysing the pressure cloud diagram reveals higher pressure on the conical pipe due to direct fluid impact at the inlet. In pipe bends, the pressure on the outer bend exceeds that on the inner bend due to fluid impact caused by velocity fluctuations, leading to energy loss. Consequently, higher water flow rates increase pipeline pressure, exacerbating energy loss and reducing dredging efficiency. Conversely, lower water flow rates result in reduced velocity fluctuations at cylindrical pipe bends, leading to lower energy loss. Thus, varying water velocities significantly impact the dredging efficiency.

3.4. Analysis of the Impact of Pipeline Diameter

The effect of the pipe inlet pipe diameter and pipe outlet pipe diameter on dredging efficiency is based on the fluid flow equation and pipe cross-sectional area formula:

$$A = \frac{\pi D^2}{4} \tag{3}$$

Available:

$$Q = \frac{\pi D^2 v}{4} \tag{4}$$

where Q is the fluid flow, unit m^3/s ; D is the pipe diameter, unit m ; and v is the fluid velocity, unit m/s .

When the relationship between the inlet flow rate Q_1 and the outlet flow rate Q_2 is $Q_1 = Q_2$, the fluid flow in the pipeline is stable. When $Q_1 > Q_2$ is met, the inlet flow rate is greater than the outlet flow rate, and the pipeline experiences a silt-clogging phenomenon. When $Q_1 < Q_2$ is met, the inlet flow rate is less than the outlet flow rate, and the pipeline will produce bubbles, affecting the mixing of the state of the water and the silt, and thereby affecting the efficiency of desilting; therefore, the inlet diameter and the outlet diameter of the pipeline will affect the efficiency of desilting.

4. Orthogonal Test Design

Orthogonal Test Factor Level Table Design

Based on the analysis of factors impacting dredging efficiency, the selection of appropriate levels for simulation experiments involved the use of five factors with five levels each. To mitigate systematic errors arising from human factors, the ordering of factor levels cannot strictly follow the magnitude of their values. Hence, a random number method is employed for sorting the various factor levels, as illustrated in Table 4.

Table 4. Table of factor levels for the simulation experiment.

Factor	Level 1	Level 2	Level 3	Level 4	Level 5
Reamer speed (rpm)	90	105	135	150	120
Arrangement angle (°)	45	40	55	35	50
Water flow speed (m/s)	1.4	0.7	2.1	1.05	1.75
Inlet pipe diameter (mm)	168	148	188	208	128
Outlet pipe diameter (mm)	66	76	36	56	46

Based on the table provided, conducting full-scale experiments would require a minimum of 3125 trials. However, employing an orthogonal experimental design significantly reduces the number of experiments needed. The key advantages of orthogonal experimental design include uniform selection, which enables the systematic selection of a

representative subset of experimental programs from all possible combinations. Statistical analysis: By analysing the results of this subset of experiments statistically, it becomes possible to identify the most effective programs. Comprehensive insight: Furthermore, an orthogonal experimental design allows for a deeper analysis of experimental outcomes, providing insights beyond the basic results obtained. These advantages collectively enhance the efficiency and effectiveness of the experimental process, saving time and resources while yielding valuable insights [21].

The orthogonal test table $L_{25}(5^5)$ and test results are shown in Table 5, where the blank column, also known as the error column, indicates that no factors or interactions are placed in the column, which is used to reduce the error; generally, a blank column is retained.

Table 5. Table $L_{25}(5^5)$ and results of orthogonal experiments.

No.	Reamer Speed A	Layout Angle B	Water Velocity C	Blank Column	Inlet Pipe Diameter D	Outlet Pipe Diameter E	Dredging Efficiency
1	90	45	1.4	1	168	66	0.8828
2	105	45	0.7	2	148	76	0.8756
3	135	45	2.1	3	188	36	0.8934
4	150	45	1.05	4	208	56	0.8633
5	120	45	1.75	5	128	46	0.9119
6	90	40	0.7	3	188	46	0.8981
7	105	40	2.1	4	208	66	0.8915
8	135	40	1.05	5	128	76	0.9243
9	150	40	1.75	1	168	36	0.9028
10	120	40	1.4	2	148	56	0.9091
11	90	55	2.1	5	128	56	0.9477
12	105	55	1.05	1	168	46	0.9174
13	135	55	1.75	2	148	66	0.8930
14	150	55	1.4	3	188	76	0.8537
15	120	55	0.7	4	208	36	0.9207
16	90	35	1.05	2	148	36	0.9258
17	105	35	1.75	3	188	56	0.8991
18	135	35	1.4	4	208	46	0.9107
19	150	35	0.7	5	128	66	0.8531
20	120	35	2.1	1	168	76	0.9403
21	90	50	1.75	4	208	76	0.9027
22	105	50	1.4	5	128	36	0.8547
23	135	50	0.7	1	168	56	0.9270
24	150	50	2.1	2	148	46	0.8225
25	120	50	1.05	3	188	66	0.8970
K1	4.5371	4.4270	4.4111	4.4495	4.5704	4.4174	
K2	4.4384	4.5259	4.4745	4.5339	4.4261	4.4966	
K3	4.5485	4.5126	4.4954	4.4757	4.4412	4.4975	
K4	4.2954	4.5290	4.5279	4.4494	4.4890	4.5463	
K5	4.5789	4.4040	4.5095	4.5099	4.4917	4.4606	
k1	0.9074	0.8854	0.8822	0.8899	0.9141	0.8835	
k2	0.8877	0.9052	0.8949	0.9068	0.8852	0.8993	
k3	0.9097	0.9025	0.8991	0.8951	0.8882	0.8995	
k4	0.8591	0.9058	0.9056	0.8899	0.8978	0.9093	
k5	0.9158	0.8808	0.9019	0.9020	0.8983	0.8921	

When analysing the results of orthogonal experiments, intuitive analysis is commonly used due to its simplicity, intuitive nature, and minimal computational requirements. However, this approach has drawbacks such as the inability to estimate the magnitude of the error or accurately gauge the importance of each factor’s influence. Moreover, intuitive analysis can be inconvenient when dealing with interactions between multilevel experiments, potentially impacting the experimental results.

To address these limitations, analysis of variance (ANOVA) is employed, offering a solution to the shortcomings of intuitive analysis. In this study, employing an orthogonal experimental design featuring five factors and five levels, and ANOVA was utilized to thoroughly analyse the experimental outcomes. This approach allows for a comprehensive examination of the variance within the data, providing insights into the significance of each factor and any interactions present.

ANOVA, as a statistical method, is able to analyse the impact of different factors on the variation in data and determine which factors have a significant impact on the variation in data, where the main parameters are as follows: 1. The sum of squares of deviations, which refers to the sum of squares of the differences between the individual numbers of a set of data and their arithmetic mean, and the sum of squares of deviations reflecting the degree of dispersion or concentration of the data in the set, the larger the S is, the more dispersed the data are in the set, and vice versa. The larger S is, the more dispersed the group is, and conversely, the more concentrated the group is. 2. Degree of freedom, which indicates the amount of free information used to calculate statistical inferences, determines the shape and parameters of the distribution (usually the F-distribution) used in the analysis of variance (ANOVA). 3. Mean sum of squares of deviations (mean squares), which allows for reasonable comparisons of the degree of dispersion or concentration of two groups of data consisting of different numbers. 4. The F-value, which refers to the mean sum of squares of the deviations caused by the change in the level of the factor with the ratio of the sum of the squares of the mean deviations due to the errors. The F-value is used to compare whether the differences are due to experimental errors or changes in the level of the factors.

The experiment was arranged using an orthogonal table $L_{25}(5^5)$ with factor levels $r = 5$, the number of orthogonal test columns $m = 5$, the total number of experiments $n = 25$, and the results of the experiment $y_i (i = 1, 2, 3 \dots, 25)$.

1. The total sum of the squared deviations is calculated, and the total sum of the squared deviations is calculated:

$$\bar{y} = \frac{1}{n} \sum_{i=1}^n y_i = 0.8967 \tag{5}$$

$$T = \sum_{i=1}^n y_i = 22.4184 \tag{6}$$

$$Q = \sum_{i=1}^n y_i^2 = 20.1249 \tag{7}$$

$$P = \frac{1}{n} \left(\sum_{i=1}^n y_i \right)^2 = \frac{T^2}{n} = 20.1034 \tag{8}$$

$$SS_T = \sum_{i=1}^n (y_i - \bar{y})^2 = \sum_{i=1}^n y_i^2 - \frac{1}{n} \left(\sum_{i=1}^n y_i \right)^2 = Q - P = 0.0215 \tag{9}$$

SS_T , which is the total sum of squared deviations, corresponds to the total variation in the experimental results, with variations in the level of the factors and experimental errors being responsible for the differences between the results.

The sum of the squared deviations due to each factor is then calculated, and for column $j (j = 1, 2, 3, 5, 6)$ of the orthogonal table, SS_j is said to be the sum of the squared deviations due to column j :

$$SS_j = \frac{n}{r} \sum_{i=1}^r (k_i - \bar{y})^2 = \frac{r}{n} \left(\sum_{i=1}^r K_i^2 \right) - \frac{T^2}{n} = \frac{r}{n} \left(\sum_{i=1}^r K_i^2 \right) - P \tag{10}$$

The results are as follows:

$$SS_A = 0.0107 \quad SS_B = 0.0028 \quad SS_C = 0.0016 \quad SS_D = 0.0025 \quad SS_E = 0.0014 \quad SS_{\text{Blank}} = 0.0008$$

Derived from the above equation:

$$SS_T = \sum_j^m SS_j \tag{11}$$

That is, the total sum-of-squares decomposition is the sum of the sum-of-squares of the columns.

Then, the sum of the squared deviations of the errors is calculated:

$$SS_e = SS_{\text{Blank}} = SS_T - \sum_j^m SS_j = 0.0008 \tag{12}$$

This finding is consistent with the calculations.

2. To calculate the degrees of freedom, first calculate the total degrees of freedom for the total sum of squares:

$$df_T = n - 1 = 24 \tag{13}$$

The degrees of freedom correspond to the sum of the squares of the departures of a given column:

$$df_j = r - 1 = 4 \tag{14}$$

Then: $df_A = df_B = df_C = df_D = df_E = 4$.

Then, there is:

$$df_T = \sum_{j=1}^n df_j \tag{15}$$

Degrees of freedom for errors:

$$df_e = \sum df_{\text{Blank}} = 4 \tag{16}$$

3. The mean sum of squared deviations (mean square) is calculated. The mean square of factor A is:

$$MS_A = \frac{SS_A}{df_A} \tag{17}$$

The mean square of the error is:

$$MS_e = \frac{SS_e}{df_e} \tag{18}$$

Then, there is:

$$MS_A = 0.002677 \quad MS_B = 0.000707 \quad MS_C = 0.000398$$

$$MS_D = 0.000636 \quad MS_E = 0.000351 \quad MS_e = 0.000197$$

If the mean square of a factor is less than or equal to the mean square of the error, it is classified as an error, thus contributing to a new error. Upon comparison with the calculations above, it is evident that the mean square of the five factors exceeds the mean square of the error. Consequently, the only error identified is the empty column.

4. The F value is calculated by dividing the mean square of each factor by the mean square of the error to obtain the F value, and the F value of factor A is:

$$F_A = \frac{MS_A}{MS_e} \tag{19}$$

Then, there is:

$$F_A = 13.619789 \quad F_B = 3.598309 \quad F_C = 2.024785 \quad F_D = 3.238761 \quad F_E = 1.785547$$

Finally, based on the F value of each factor, by finding the critical value $\alpha = 0.05$ of the given significance level $F_{\alpha}(4, 19) = 2.740$ in the F-distribution table and comparing the magnitude of the F-value and the critical value, the following results are obtained:

$$F_A > F_{\alpha}, F_B > F_{\alpha}, F_D > F_{\alpha}, F_C < F_{\alpha}, F_E < F_{\alpha}$$

The analysis revealed that factors A, B, and D exerted a notable influence on the experimental outcomes, with factor A exhibiting the most significant impact. Conversely, factors C and E had no significant effect on the experimental results. These findings are summarized in the analysis of variance (ANOVA) Table 6.

Table 6. ANOVA table.

Source of Variation	SS	df	MS	F	Significance
A	0.0107	4	0.002677	13.619789	**
B	0.0028	4	0.000707	3.598309	**
C	0.0016	4	0.000398	2.024785	*
D	0.0025	4	0.000636	3.238761	**
E	0.0014	4	0.000351	1.785547	*
Inaccuracies	0.0008	4	0.000197		
Aggregate	0.0199	24			

* denotes significance, with a higher number of *'s indicating a higher significance of the factor.

Based on the results of the orthogonal test design and without considering interactions, the optimal program is determined by selecting the maximum K value corresponding to each factor's level, denoted as $A_5B_4C_4D_1E_4$. This translates to setting the rotational speed to 120 rpm, the angle of the winch suction device arrangement to 35° , the water flow rate to 1.05 m/s, the inlet diameter to 168 mm, and the outlet diameter of the pipe to 56 mm. As mentioned earlier, when setting up the initial simulation experiment, the settings are as follows: reamer rotation speed of 60 rpm, reamer arrangement angle of 45° , pump pipe outlet water velocity of 1.3 m/s, connecting silo pipe diameter of 168 mm, outlet pipe diameter of 56 mm, through the simulation test, the dredging efficiency of about 0.83538. The parameter settings with the results of the optimal solution determined by orthogonal test have a big difference! At the same time, comparing Table 5, it can be found that there is no optimal programme group in the 25 groups of the orthogonal test, so the optimal programme determined by the experimental results has not been verified by simulation; in order to maintain scientific rigor, it is necessary to verify whether the optimal results of the orthogonal test are better than the other results of the test, so the optimal programme is set up for the simulation, and the result is shown in Figure 12.

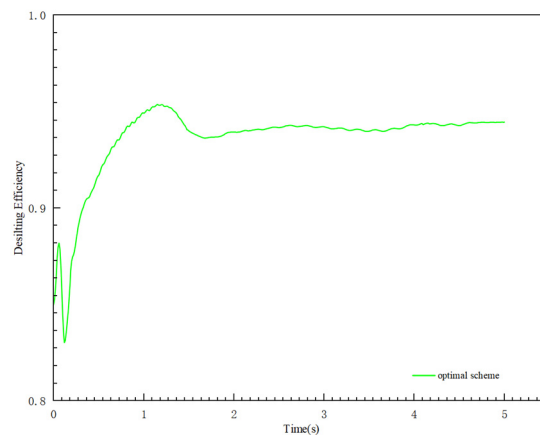


Figure 12. Optimal solution group test results.

According to the experimental results of the verified optimal scheme group, it can be seen that the dredging efficiency is 0.94439, which is higher than all the results of the 25 groups of experiments in the orthogonal test, so the experimental results of this group are the optimal results, which indicates that the orthogonal experimental design is scientific and reasonable, and comparing with the results of the initial experimental setup, the dredging efficiency has been increased by 13.049%, and the power consumption of the mud pump has been decreased by 19.23%.

5. Conclusions

This paper presents the design of a winch suction underwater dredging robot and establishes a computational fluid dynamics simulation model for an underwater winch suction device. The analysis identified five key factors influencing dredging efficiency: the reamer rotational speed, the angle of the winch suction device arrangement, the water velocity, the inlet pipe diameter, and the outlet pipe diameter. Orthogonal testing is employed to optimize these factors, significantly reducing the number of tests from 3100 to 25.

The results of the orthogonal test, analysed using ANOVA, indicate that the reamer rotational speed, reamer and suction device layout angle, and inlet pipe diameter have a significant impact on the desilting efficiency. Based on these findings, the optimal program is determined by setting the rotational speed to 120 rpm, the winch suction device angle to 35°, the water flow rate to 1.05 m/s, the inlet diameter to 168 mm, and the outlet diameter of the pipe to 56 mm.

Subsequent simulation tests confirm the effectiveness of the optimal scheme, yielding a dredging efficiency of 0.94439. Compared to the initial test setup, this represents a 13.049% increase in dredging efficiency and a 19.23% reduction in the power consumption of the sludge pump, thus enhancing overall dredging performance.

6. Patents

Two patent applications based on the research in this paper were filed and accepted on 23 December 2023 under application numbers 202323523066.2 and 202323523064.3.

Author Contributions: Conceptualization, L.W., Y.K. and L.S.; methodology, Y.K. and Y.W.; software Y.K., Z.Z. and R.C.; validation, L.W., Y.K., Y.W. and Z.Z., formal analysis, Y.K.; investigation, Y.K. and Y.W.; resources, Y.K. and L.W.; data curation, Y.K.; writing—original draft preparation, Y.K.; writing—review and editing, Y.K.; visualization, Y.W. and X.S.; supervision, L.W. and R.C.; project administration, L.W., D.X. and L.S.; funding acquisition, L.W., D.X. and Y.K.; All authors have read and agreed to the published version of the manuscript.

Funding: This research was supported by “ZHONGYUAN Talent Program” (ZYYCYU202012112), Foreign Expert Project of Ministry of Science and Technology of the People’s Republic of China (G2023026004L), Water Conservancy Equipment and Intelligent Operation & Maintenance Engineering Technology Research Centre in Henan Province (Yukeshi2024-01), Henan International Joint Laboratory of Thermo-Fluid Electro Chemical System for New Energy Vehicle (Yuke2020-23). The Scientific and Technological Project of Henan Province: (NO. 232102211035); Fund of Innovative Education Program for Graduate Students at NCWU (NCWUYC-202315082).

Institutional Review Board Statement: Not applicable.

Informed Consent Statement: Not applicable.

Data Availability Statement: Data are contained within the article.

Conflicts of Interest: Author Liyang Shang was employed by Yellow River Machinery Co., Ltd. The remaining authors declare that the research was conducted in the absence of any commercial or financial relationships that could be construed as a potential conflict of interest.

References

1. Huang, Y.H.; Zhu, W.; Qian, X.D.; Zhang, N.; Zhou, X.Z. Change of mechanical behavior between solidified and remolded solidified dredged materials. *Eng. Geol.* **2011**, *119*, 112–119. [[CrossRef](#)]
2. Yan, J.L.; Li, F. Effects of sediment dredging on freshwater system: A comprehensive review. *Environ. Sci. Pollut. Res.* **2023**, *30*, 119612–119626. [[CrossRef](#)]
3. Chen, Q.; Ran, F.Y.; Wei, Q.; Zheng, X.Y.; Zhao, M.; Liu, S.H.; Wang, L.J.; Fan, C.Z. A Review on Dewatering of Dredged Sediment in Water Bodies by Flocculation Processes. *Water Air Soil Pollut.* **2024**, *235*, 67. [[CrossRef](#)]
4. Zhang, J.L.; Shang, Y.Z.; Liu, J.Y.; Lu, J.; Wei, S.T.; Wan, Z.W.; Luo, Q.S.; Chen, C.X.; Tong, L.; Wang, Q.; et al. Optimisation of reservoir operation mode to improve sediment transport capacity of silt-laden rivers. *J. Hydrol.* **2021**, *594*, 125951. [[CrossRef](#)]
5. Hou, C.Y.; Yi, Y.J.; Song, J.; Zhou, Y. Effect of water-sediment regulation operation on sediment grain size and nutrient content in the lower Yellow River. *J. Clean. Prod.* **2021**, *279*, 123533. [[CrossRef](#)]
6. Beijing Municipal Water Affairs Bureau. Available online: <https://swj.beijing.gov.cn/swdt/> (accessed on 20 March 2024).
7. Liu, M.; Yang, Y.; Shao, Z.; Liu, Y.; Wang, Z.; Chen, Z.; Chen, M.; Jiao, L.; Song, D.; Li, J.; et al. Effects of Dredging on Nitrogen and Phosphorus Storage Patterns and Retention Mechanisms in Column Core Sediments in the Caohai Region of Dianchi Lake. *Water* **2024**, *16*, 449. [[CrossRef](#)]
8. Chen, J.; Xie, P.; Ma, Z.; Niu, Y.; Tao, M.; Deng, X.; Wang, Q. A systematic study on spatial and seasonal patterns of eight taste and odor compounds with relation to various biotic and abiotic parameters in Gonghu Bay of Lake Taihu, China. *Sci. Total Environ.* **2010**, *409*, 314–325. [[CrossRef](#)] [[PubMed](#)]
9. Hu, P.; Deng, S.; Zhao, Z.; Cao, Z.; Liu, H. Dredging Volume Estimation and Dredging Timing for Waterway Maintenance: A Case Study Using a Depth-Averaged Hydrosediment-Morphodynamic Model with Transient Dredging Effects. *J. Waterw. Port Coast. Ocean. Eng.* **2022**, *148*, 04022014. [[CrossRef](#)]
10. Wu, Q.X.; Yang, X.C.; Wu, Y.; Zhou, Z.J.; Wang, J.; Zhang, B.T.; Luo, Y.B.; Chepinskiy, S.A.; Zhilenkov, A.A. A novel underwater bipedal walking soft robot bio-inspired by the coconut octopus. *Bioinspiration Biomim.* **2021**, *16*, 046007. [[CrossRef](#)]
11. Khan, A.; Wang, L.; Gang, W.; Imran, M.; Waqas, H.M.; Zaidi, A.A. Concept Design of the Underwater Manned Seabed Walking Robot. *J. Mar. Sci. Eng.* **2019**, *7*, 366. [[CrossRef](#)]
12. Yang, L.; Zhao, S.; Wang, X.; Shen, P.; Zhang, T. Deep-Sea Underwater Cooperative Operation of Manned/Unmanned Submersible and Surface Vehicles for Different Application Scenarios. *J. Mar. Sci. Eng.* **2022**, *10*, 909. [[CrossRef](#)]
13. Cepeda, M.F.S.; Machado, M.d.S.F.; Barbosa, F.H.S.; Moreira, D.S.S.; Almansa, M.J.L.; de Souza, M.I.L.; Caprace, J.-D. Exploring Autonomous and Remotely Operated Vehicles in Offshore Structure Inspections. *J. Mar. Sci. Eng.* **2023**, *11*, 2172. [[CrossRef](#)]
14. Ngatini; Apriliani, E.; Nurhadi, H. Ensemble and Fuzzy Kalman Filter for position estimation of an autonomous underwater vehicle based on dynamical system of AUV motion. *Expert Syst. Appl.* **2017**, *68*, 29–35. [[CrossRef](#)]
15. Given, D.W. ROV Technology Trends And Forecast. In Proceedings of the Proceedings OCEANS '83, San Francisco, CA, USA, 29 August–1 September 1983.
16. Louis, L.W.; Jonathan, C.H.; David, A.S.; Dana, R.Y.; Timothy, E.T. A New Control System for the Next Generation of US and UK Deep Submergence Oceanographic ROVS. *IEAC Proc. Vol.* **2003**, *36*, 133–138. [[CrossRef](#)]
17. Rozman, B.J.; Utyakov, L.L. Micro ROV underwater observations. In Proceedings of the Oceans '99. MTS/IEEE. Riding the Crest into the 21st Century. Conference and Exhibition. Conference Proceedings (IEEE Cat. No.99CH37008), Seattle, WA, USA, 13–16 September 1999; pp. 1542–1543.
18. Snyder, J. Doppler Velocity Log Navigation For Observation-Class ROVs. *Sea Technol.* **2010**, *51*, 27–30.
19. Chen, Q.; Liu, Z. A novel voltage regulation strategy for the electric power delivery system of a 6000-m ROV. *Appl. Ocean. Res.* **2018**, *80*, 112–117. [[CrossRef](#)]
20. He, D.; Chen, S.; Bai, B. Experiment and Numerical Simulation on Gas-Liquid Annular Flow through a Cone Sensor. *Sensors* **2018**, *18*, 2923. [[CrossRef](#)] [[PubMed](#)]
21. Wang, L.; Jiang, S.; Ping, D.; Feng, W.; Shang, L.; Tian, B.; Xu, D. Performance Optimization of Underwater Crushing Unit Based on AHP. *J. Mar. Sci. Eng.* **2023**, *11*, 1536. [[CrossRef](#)]

Disclaimer/Publisher's Note: The statements, opinions and data contained in all publications are solely those of the individual author(s) and contributor(s) and not of MDPI and/or the editor(s). MDPI and/or the editor(s) disclaim responsibility for any injury to people or property resulting from any ideas, methods, instructions or products referred to in the content.